


Article

Investigation of Compact Hollow-Anode Discharge Source for Copper Thin Films by Sputtering Processes

In-Je Kang ^{1,*} , Ji-Hun Kim ¹, In-Sun Park ²  and Kyu-Sun Chung ²¹ Institute of Plasma Technology, Korea Institute of Fusion Energy, Gunsan 54004, Korea; jhkim75@kfe.re.kr² Department of Electrical Engineering, Hanyang University, Seoul 133791, Korea; parkis930@hanyang.ac.kr (I.-S.P.); kschung@hanyang.ac.kr (K.-S.C.)

* Correspondence: ij kang@kfe.re.kr

Abstract: A compact hollow-anode discharge (HAD) source with a size of 60 mm in radius and 70 mm in length has been developed to stably generate plasma jets for various sputtering processes in semiconductor and display fabrications. A developed HAD plasma source has been investigated by cylindrical electric probes, and the experimental results were compared to the values of numerical calculations. A uniform density discharge model with a geometry factor was proposed to estimate the profiles of plasma parameters. Owing to the difference of absolute magnitude, even with the similar trend of spatial variation, plasma parameters such as electron temperature (T_e) and plasma density (n_e) measured at $z = 3$ cm have been calibrated by the values of numerical calculations at the nozzle entrance ($z = 0$ cm, at the throat of the jet), and the calibration factors for T_e and n_0 have been deduced by comparing the experimental values to numerical calculations. These are to be explained by the decay mechanism along the axis of the jet with elastic collisions in terms of the mean free path. The developed HAD plasma source was tested for the deposition of Cu thin films with an optimized condition as a plausible application to sputtering processes.



Citation: Kang, I.-J.; Kim, J.-H.; Park, I.-S.; Chung, K.-S. Investigation of Compact Hollow-Anode Discharge Source for Copper Thin Films by Sputtering Processes. *Energies* **2021**, *14*, 3138. <https://doi.org/10.3390/en14113138>

Academic Editor: I. M. Dharmadasa

Received: 13 April 2021

Accepted: 23 May 2021

Published: 27 May 2021

Publisher's Note: MDPI stays neutral with regard to jurisdictional claims in published maps and institutional affiliations.



Copyright: © 2021 by the authors. Licensee MDPI, Basel, Switzerland. This article is an open access article distributed under the terms and conditions of the Creative Commons Attribution (CC BY) license (<https://creativecommons.org/licenses/by/4.0/>).

Keywords: hollow anode discharge source; uniform density discharge model; copper thin films

1. Introduction

Plasma jets or ion beam sources have been developed for various material applications, such as plasma enhanced chemical vapor deposition (PECVD), dry etching and plasma surface treatments to improve qualities of substrates and efficiency of processing [1–4]. A hollow-anode discharge (HAD) source invented by Miljevic [5] was proposed as a plasma source for generating plasma jets. It has provided high-density and high-energy electrons in the hollow-anode region. This is because the probability for collisions of electrons with atoms increases when passing through the hollow anode, and the intensive ionization and excitation of the atoms can be observed [5,6]. As a DC plasma source, it has the advantage of easy operation, low cost and high homogeneity [7]. However, analysis of plasma jets from the hollow-anode plasma is insufficient for material applications, and more practical data are needed in addition to previous research, due to the lack of measurements of plasma parameters and comparison with theory [5,6,8,9].

In this work, a compact HAD source has been developed to stably generate plasma jets for sputtering processes. A uniform density discharge model [10] has been introduced for estimating profiles of the plasma parameters of a present plasma source. The characteristics of the plasma parameters inside plasma jets with various operating conditions were experimentally investigated using IV characteristics measured by cylindrical probes. Experimental results were compared with values of numerical calculations to check the applicability of the developed plasma source, according to the uniform density model for various sputtering processes.

2. Model

To estimate electron temperature (T_e) and plasma density (n_e) in a cylindrical discharge reactor, a uniform density discharge model by Lieberman is considered [10]. This model assumes a uniform density in the cylindrical plasmas with a sharp boundary at the sheath edge (i.e., a box shape). Electrons as the major energy carrier are assumed to have the Maxwell–Boltzmann distribution. T_e is calculated using the particle balance between the total surface particle losses and the total volume ionization, while n_e is calculated using an energy balance between the total power absorbed and the total power losses. Considering the particle balance to determine T_e , the equilibrium equation is given as [10]:

$$n_0 u_B A_{eff} = \eta_{iz} n_g n_0 \pi R^2 L, \quad (1)$$

where $A_{eff} = 2\pi R^2 h_L + 2\pi R L h_R$ is the effective area for particle losses. n_0 , u_B , η_{iz} , n_g , R , and L are the plasma density of the central reactor region, Bohm speed, the ionization rate constant, the neutral gas density, radius and axial length of the chamber, respectively. Using the definition of the Bohm speed, $u_B = (T_e/m_i)^{1/2}$ where m_i is the mass of an ion, the electron temperature can be obtained as:

$$T_e = m_i u_B^2 = m_i \left(\frac{\pi R^2 L}{A_{eff}} n_g \eta_{iz} \right)^2 = m_i n_g^2 \eta_{iz}^2 \xi_{eff}^2, \quad (2)$$

where ξ_{eff} is an effective plasma size for particle losses, which is given as $\xi_{eff} \equiv \pi R^2 L / A_{eff} = 0.5RL / (Rh_L + Lh_R)$. It can be estimated using Godyak's formulae of h_L and h_R : $h_L \equiv n_{sL} / n_0 \approx 0.86(3 + L/2\lambda_i)^{-1/2}$ for the axial sheath edge density (n_{sL}) and $h_R \equiv n_{sR} / n_0 \approx 0.8(4 + R/2\lambda_i)^{-1/2}$ for the radial sheath density (n_{sR}), where λ_i is ion mean free path [10–12]. The ionization rate constant is given as [10]:

$$\eta_{iz} = \sigma_0 \bar{v}_e \left(1 + \frac{2T_e}{E_{iz}} \right) e^{-E_{iz}/T_e}, \quad (3)$$

where $\sigma_0 = \pi \left(\frac{1}{4\pi\epsilon_0 E_{iz}} \right)^2$ is the initial condition for the Thomson cross-section, and $\bar{v}_e = \left(\frac{8T_e}{\pi m} \right)^{1/2}$ is the average electron speed. E_{iz} and ϵ_0 are the ionization energy of gas and permittivity of free space, respectively. The uniform density model assumes the sharp fall near the wall, while the practical plasma density profile would follow a Gaussian distribution. Between the uniform distribution and the Gaussian distribution, there is a non-negligible and physically important difference: Uniform distribution assumes that the density at the boundary or at the sheath is the same as the density of the center or equilibrium (n_0) by assuming that the sheath potential is the same as the plasma potential ($V_s = V_p : n_e(r=s) = n_0 \exp[V_s - V_p] = n_0$). This is a common assumption that Child, Langmuir, Chen, Franklin and Lieberman have already made [10,13]. However, the real boundary condition at the sheath is the Bohm condition, i.e., the ion speed at the sheath is the Bohm speed ($u_B = (T_e/m_i)^{1/2}$) if $T_i = 0$, which leads to the sheath potential, which should be such that $V_s - V_p = -T_e/2e$, which again makes the sheath density $n_s = n_0/2$. Thus, under Bohm's criterion [10,13,14], the boundary density or sheath density should not be n_0 , but rather $n_0/2$, which makes the uniform source distribution unacceptable, physically [14]. Therefore, although a Gaussian profile is not the only physical one, it would be a better one than the uniform profile. By assuming a Gaussian distribution for a plasma density profile, this indicates that plasma particle losses are smaller than those of the uniform density model as shown in Figure 1. Therefore, to compensate for the difference of loss of particles and energy between the uniform and Gaussian models, we need to introduce a geometry factor (k) to the uniform model by reducing the effective area of loss (A_{eff}), or by increasing effective plasma size (ξ_{eff}). The effect of k is to be shown in

the results of numerical calculations for plasma density and electron temperature. From Equation (2), T_e can be rewritten as:

$$T_e = m_i n_g^2 \eta_{iz}^2 \left(\frac{\xi_{eff}}{k} \right)^2. \quad (4)$$

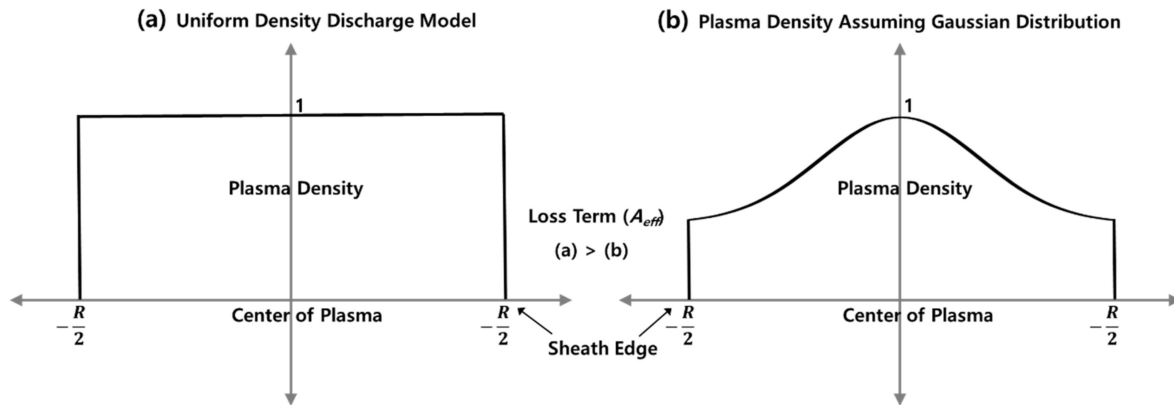


Figure 1. Comparison of plasma density distribution for the complement of A_{eff} for plasma particle losses: (a) uniform density discharge model and (b) plasma density assuming Gaussian distribution.

Assuming uniform energy loss at all surfaces, plasma density (n_0 , in the central region of plasma source) from the energy balance can be calculated by equating the total power generation (P_g), which is absorbed into the electrons [10]:

$$P_g = n_0 u_B A_{eff} E_T, \quad (5)$$

where total energy loss (E_T) is given as $E_T = E_i + E_e + E_c$ [eV] and the other constants are the same as mentioned previously. Mean kinetic energy loss per ion loss, E_i , is given as $V_s + 0.5T_e$ for argon gas. $V_s = T_e \ln(m_i/2\pi m_e)^{1/2}$ is the sheath voltage, where m_e is the mass of an electron when ion and electron fluxes which are balanced in the steady state are assumed. Mean kinetic energy loss per electron loss, E_e , is approximated as $2T_e$. Collisional energy loss per electron–ion pair created (E_c) is indicated as [10]:

$$E_c = [\eta_{iz} E_{iz} + \eta_{ex} E_{ex} + \eta_{el} (3m_e/m_i) T_e] / \eta_{iz}, \quad (6)$$

where η_{iz} , η_{ex} , η_{el} and E_{ex} are rate constants for ionization, excitation, elastic scattering and excitation energy, respectively. In the RHS of Equation (6), the numerator means collisional energy losses due to ionization, excitation and elastic scattering against neutral atoms. Finally, for estimation of n_0 , Equation (5) is rewritten as:

$$n_0 = P_g / E_T A_{eff} (T_e / m_i)^{1/2}, \quad (7)$$

where T_e for calculation of u_B is used from Equation (4), where k is applied to check its effects for the compensation of A_{eff} for plasma particle losses. To simulate plasma parameters, the discharge current between electrodes was assumed to be given by the Child–Langmuir space-charge limited equation [10,15,16], along with the following conditions: radius of cylindrical source (R) = 10 mm, axial length (L) = 10 mm and argon gas as working gas.

3. Experiment

The operating principle, schematic view and photograph of the developed HAD source for generating plasma jets with the experimental set-up are shown as Figures 2 and 3. The developed source has a compact size with a length of 70 mm and radius of 60 mm.

The cathode of HAD has a hemisphere shape with a diameter of 20 mm, while the anode has a narrow throat with a diameter of 3 mm and a wide exit with 9 mm in diameter. Oxygen-free electrolytic coppers (OFC) are used for electrodes. To cover 98% of the anode area, excluding the nozzle vicinity, a Teflon (PTFE) insulator between electrodes is used with a thickness of 3 mm. A water-cooling system is introduced inside the cathode to prevent and reduce thermal damage from plasmas. Argon gases are fed into the plasma source, where the pressure is approximately 100 Pa (0.8 Torr) at a flow rate in a 1–100 sccm range, through a stainless tube fixed by vacuum fitting. Figure 3b is a photograph of the plasma source after fabrication. The exposed anode area for generating hollow-anode plasma at the nearby nozzle throat, such as a plasma ball [6], is about 13 mm². For the ignition of plasmas between electrodes, the DC power was supplied to electrodes with an applied voltage of 0–450 V and a discharge current of 0–150 mA.

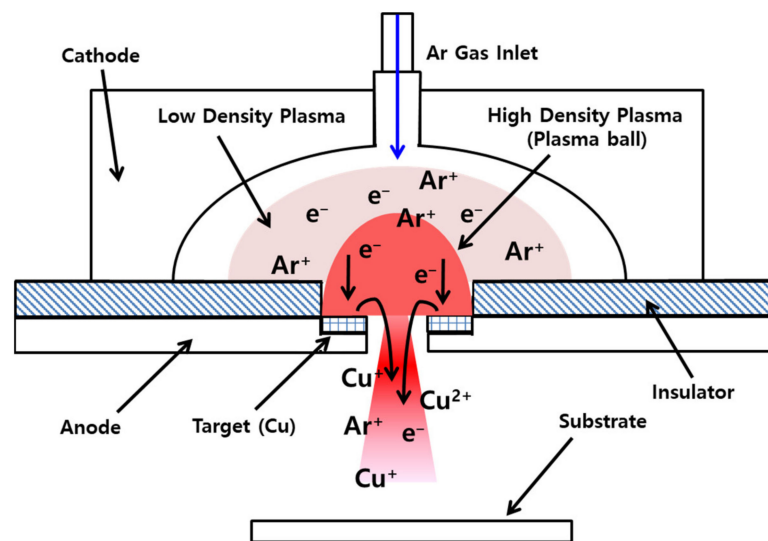


Figure 2. Principle of hollow-anode plasma source for sputtering processes. It uses a high-density plasma (plasma ball) formed near a hollow and after an applied voltage transition.

At 0.4–7 Pa ($3\sim 5 \times 10^{-3}$ Torr), parameters such as T_e and n_e inside plasma jets generated from the nozzle throat were measured by cylindrical scanning probes [17,18], which were made of a molybdenum tip with 0.5×3 mm (dia. \times length) and an Al_2O_3 ceramic holder with 3 mm of diameter. The current–voltage (IV) characteristic curve is obtained from collected ion and electron currents by sweeping the probe bias voltage from -100 V to $+100$ V for the measurement of scanning the probe system with a single probe tip, as shown in Figure 3b. T_e is obtained from the slope of the IV characteristic curve, and n_e can be determined from the ion saturation current ($I_{sat} = \alpha n_e e A_s \sqrt{KT_e/m_i}$) with an assumption of $T_e \gg T_i$ at non-thermal plasma, where α , e , A_s and K are coefficients for the collective ion saturation current, electron charge, sheath area and Boltzmann constant, respectively. $A_s \approx A_p$ (probe tip area $\approx 2 \times 10^{-4}$ cm²) is assumed and $\alpha \approx 0.61$ is used for un-magnetized plasmas [19,20]. To reduce the signal uncertainty, two cylindrical probes are used, as shown in Figure 3. One scans for radial direction and the other scans for axial direction. The average value of plasma parameters measured from two cylindrical probes is used.

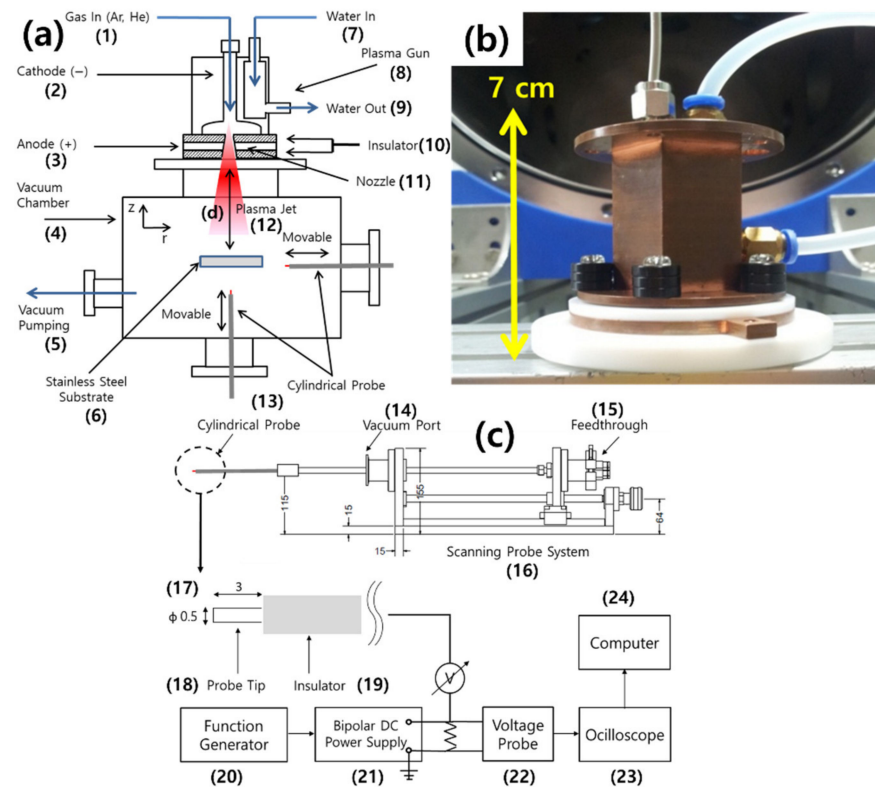


Figure 3. (a) Schematic view of a source system, (b) photograph of the developed source and (c) scanning probe system with the electric probe for measurement of plasma parameters. The distance (d) is 3 cm between the nozzle and substrate. (1) Gas in, (2) cathode, (3) anode, (4) vacuum chamber, (5) vacuum pumping, (6) stainless steel substrate, (7) water in, (8) plasma gun, (9) water out, (10) insulator, (11) nozzle, (12) plasma jet, (13) cylindrical probe, (14) vacuum port, (15) feedthrough, (16) scanning probe system, (17) 0.5×3 mm (dia. \times length), (18) probe tip, (19) insulator, (20) function generator, (21) bipolar DC power supply, (22) voltage probe, (23) oscilloscope and (24) computer.

4. Results

Figure 4 shows the VI characteristics of the plasma jets with various gas flow rates. At each specified gas flow rate, one voltage transition occurred within a specified threshold of the applied voltage, which was increased as gas flow rates decreased. After the voltage transition, generated plasma jets became more stable with high discharge currents. Applied voltages were maintained as almost constant, even when discharge currents increased up to 150 mA, showing fully developed state plasmas between the electrodes. This may be explained by a “layered-glow mode” which plays a crucial role on the relation of higher discharge currents with applied voltages only at a hollow-anode plasma source [9]. Hence, we intensively focused on plasma jets, generated by the high current mode, after voltage transition.

Figure 5a shows the experimental results of T_e measured by a cylindrical electric probe, which are to be compared to values of numerical calculations according to gas flow rates. The various k values were checked, such as $k = 0.1$ –1, e.g., $k = 0.5$ means that the amount of plasma particle losses is half that of those by the uniform density model ($k = 1$). Comparing this to the original uniform density discharge model by applying $k = 0.1$, the absolute simulated T_e values come closer to the experimental results with similar tendencies than the original model (i.e., $k = 1$) but need further analysis to optimize the model. Increasing gas flow rates produced lower T_e of the plasma jets. Significant effects of discharge currents on T_e are not observed, as shown in Figure 5b. In our developed HAD source, T_e was nearly saturated at approximately 0.45 eV at the gas flow rate of 75 sccm, irrespective of the geometry factor k . Experimental results showed lower electron temperatures than values of numerical calculations, which clearly seems to be caused by the difference of position for

the numerical calculations from that of the experimental measurement by an electric probe. The value of numerical calculations was given at the center of plasma source ($z = 0$ cm), while the one measured is at the middle of plasma jet ($z = 3$ cm) generated from the nozzle.

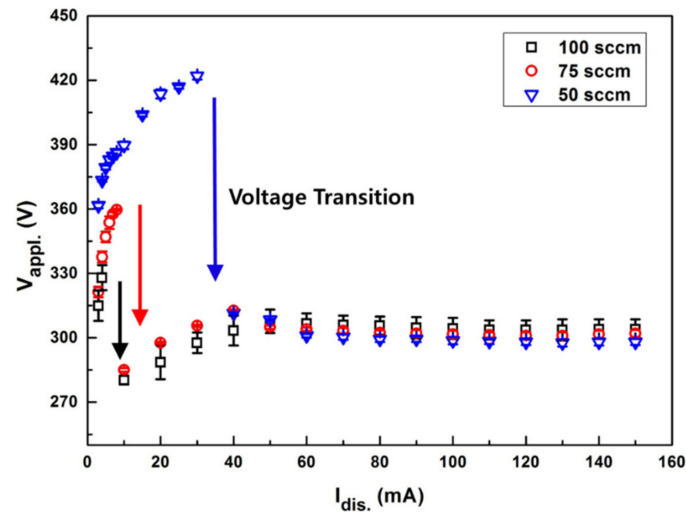


Figure 4. VI characteristics (applied voltage vs. discharge current) of the developed plasma source with various gas flow rates.

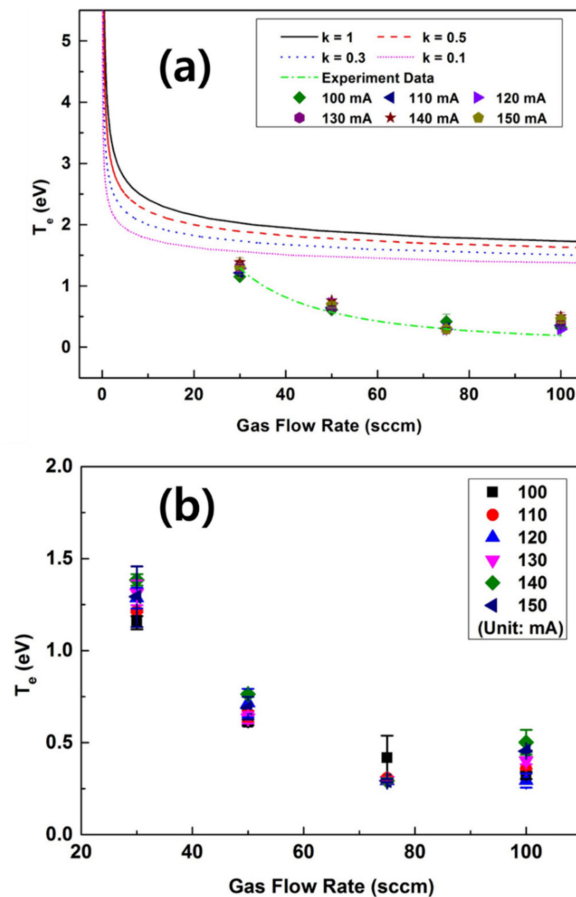


Figure 5. The T_e profiles according to gas flow rates: (a) for comparing numerical calculations with the geometry factor ($k = 0.1$ – 1) ($z = 0$ cm, at a center of plasma source) and experimental results ($z = 3$ cm, at plasma jet: 3 cm from a nozzle throat) and (b) experimental results with various discharge currents in detail.

To compensate for the difference due to the positions of measurement and numerical calculations, a calibration factor (CF_T) is introduced to T_e profiles as $CF_T = T_e(z_0, simulation) / T_e(z_{3cm}, experiment)$. By using the T_e profiles given as functions of distance (z) from the nozzle, a calibration factor is obtained, as shown in Figure 6a. The calibration factor for T_e (CF_T) is given by taking the average of the ratio: $CF_T \approx 4$. As for the calibration factors of T_e (CF_T), one could consider the small angle elastic scattering of charged particles via Coulomb collisions [21], where the ratios of different collision frequencies are given in terms of momentum relaxation rates ($\nu_m/\nu_0^{e/i}$) and energy relaxation rates ($\nu_\varepsilon/\nu_0^{e/i}$) as the following: $\nu_m^{e/i}/\nu_0^{e/i} = 1$, $\nu_m^{e/e}/\nu_0^{e/i} = 1.2$, $\nu_\varepsilon^{e/i}/\nu_0^{e/i} = 2(m_e/m_i) \sim 10^{-4}$ and $\nu_\varepsilon^{e/e}/\nu_0^{e/i} = 0.6$, where ν is the elastic collision frequency. Then, the ratio of total energy transfer to total momentum (velocity) transfer is calculated as $\nu_m/\nu_\varepsilon = (\nu_m^{e/e} + \nu_m^{e/i}) / (\nu_\varepsilon^{e/e} + \nu_\varepsilon^{e/i}) = 3.7$. Since the mean free path is inversely proportional to the collision frequency ($\lambda_n \propto 1/\nu$), the spatial variation of electron temperature can be expressed as:

$$T(z) = T_0 \exp[-z/\lambda_T] = T_0 \exp[-z/\{(\nu_m/\nu_\varepsilon)\lambda_n\}]. \quad (8)$$

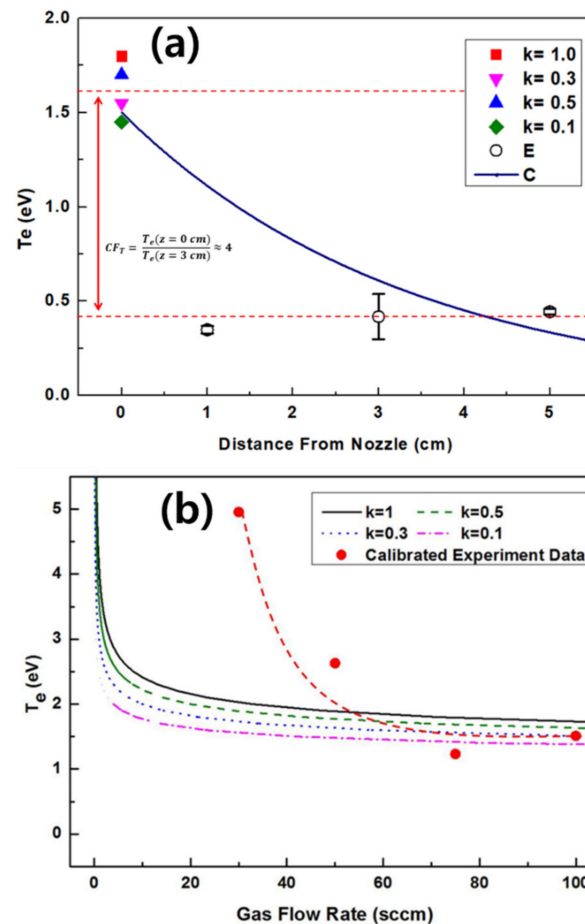


Figure 6. The T_e profiles: (a) according to distance from nozzle (argon gas flow rate: 75 sccm) to calibrate position difference for correct comparison of numerical calculation results with experiment data and (b) comparison of numerical calculation results with calibrated experiment average values of 100–150 mA as function of gas flow rates compensated for position difference (z : 0 cm). (E) and (C) in this figure legend are experiment and calculation results by Equation (8), respectively.

Hence, the calibration factor of electron temperature is calculated as $CF_T = T_0/T_{3cm} = 2.5$, which is close to our experimental calibration factor of electron temperature, $CF_T \sim 4$. Here $z = 3$ cm, $\nu_m/\nu_\varepsilon = 3.7$ and $\lambda_n = 0.9$ cm are used. Similar values of calibration

factors between the numerical calculations and experiments indicate our approach as being valid and relevant. Figure 6b shows the compensated T_e profiles comparing experimental data with values of numerical calculations, showing a similar scale and trend, yet there is another difference in terms of the gas flow rate, which is for the refinement of the present layered-glows model, with inclusion of the tremendous loss of electron energies by frequent collisions at low discharge voltages.

The profiles of plasma density, the numerical calculation results of the center of plasma source and the measurement data at 3 cm from a nozzle throat, which depend on the discharge currents with various gas flow rates, are shown in Figure 7. In comparison with the numerical calculation values, the experimental results were more dependent on gas flow rates. Plasma density measured by a cylindrical probe, which was slightly increased by raising discharge currents, shows a similar tendency with numerical calculation results. To check the effects of k to n_0 , the numerical calculation values in Figure 7a are magnified as shown in Figure 7b. By comparing the difference of experimental data with the numerical calculation values, the effects of k seem to be insignificant, but n_0 slightly increases as much as k decreases. Based on Figures 6b and 7b, it does affect the analytic values of electron temperature and density: $\Delta T_e / \text{avg. } T_e \sim 0.25 = 25\%$ and $\Delta n_0 / \text{avg. } n_0 \sim 0.1 = 10\%$. Thus, the k factor seems to affect the numerical calculation results of electron temperature more than those of density. The difference of absolute values between numerical calculations and experimental results is for the same reasons as with T_e as mentioned above, i.e., the difference of measured and simulated positions. To easily understand the reason and calibrate n_e profiles for position difference, the relation between the n_0 and n_e according to distances (1 cm, 3 cm and 5 cm) from the nozzle throat is shown in Figure 8a. As a function of the distance from the nozzle, n_0 profiles seem to be in exponential decay. This means that calibration is required for the correct comparison of experiment data with numerical calculation values at the same position. The calibration factor for n_0 is given by taking the average of the ratio: $CF_n = n_0(z_0, \text{simulation}) / n_e(z_{3\text{cm}}, \text{experiment}) \approx 30$. Calibrated experimental data seem to be fairly matched with numerical calculation results, as shown in Figure 8b. As for the calibration factors of T_e and n_e (CF_T and CF_n), one could expect the exponential decay of density and temperature along the axial direction of jets due to collisions since the density of plasma jets is strongly dependent on the mean free path (λ_n) which could be expressed as

$$n(z) = n_0 \exp[-z/\lambda_n], \quad (9)$$

where n_0 is the density at the exit of the plasma jet ($z = 0$). Applying the relation by Liebermann for the mean free path $\lambda_n = 1/330p$ (p in Torr, λ_n in cm) at $T_i \sim 0.01$ eV [10,22] to our experimental condition (gas flow rate: 75 sccm at 3.5×10^{-3} Torr), which is nonthermal plasma with low energy ions, we can obtain the calibration factor of the density profile as $CF_n = n_0/n_{3\text{cm}} = 32$. This is very close to our experimental calibration factor of plasma density, $CF_n \sim 30$. From this calibration factor, one can deduce the mean free path as the following: $\lambda_n = z / \ln(n_0/n_{3\text{cm}}) = 3 / \ln(30) = 0.9$ cm.

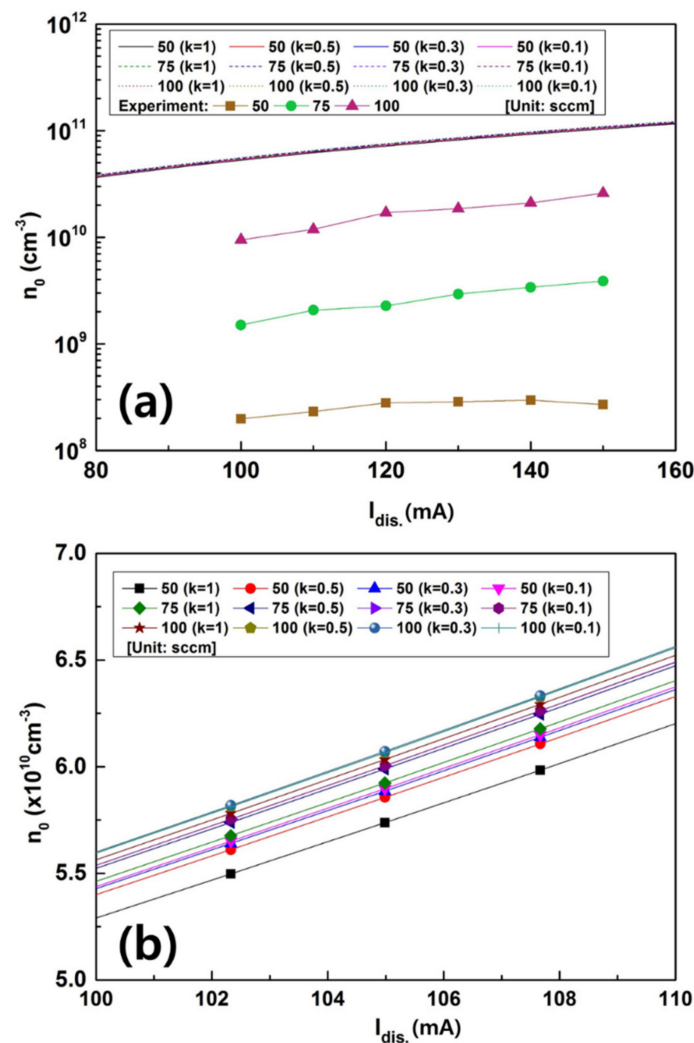


Figure 7. (a) The n_0 profiles as a function of discharge currents with various gas flow rates for comparing numerical calculations (z : 0 cm, at a center of plasma source and k : 0.1–1) and experimental results (z : 3 cm, at plasma jet from a nozzle exit) and (b) numerical calculation results in detail.

Finally, the applicability of the developed plasma source was checked for sputtering processes. Figure 9 shows the formation of the plasma jets produced by using a DC power, a pulsed DC power and a RF power for material application such as metal thin films. The deposition of copper thin films on a stainless-steel substrate with the operating source condition is given as the following: $n_e \sim 3 \times 10^9 \text{ cm}^{-3}$; $T_e \sim 0.45 \text{ eV}$ at 3 cm from the nozzle exit; gas flow rate $\sim 75 \text{ sccm}$, discharge currents $\sim 150 \text{ mA}$ and the applied voltage $\sim 300 \text{ V}$. From the etched target disc, as shown in Figure 9d, we predict that the efficiency of sputtering processes by ions generated from Cu, Pt, ITO or the other metal target discs could be improved. This is because this concept uses higher-density plasmas near a hole of anode, rather than a commercial source used by glow discharge plasmas. This is explained by the formation of stable plasma jets with a high discharge current after the voltage transition, in the section of VI characteristics. Additionally, the report [9] of experimental analyses on the plasma phenomena inside the hollow-anode discharge source to maintain the discharge at a higher sustaining current, with high efficiency in constricted DC plasmas, is a clearer rationale for improving the efficiency of sputtering processes by the developed plasma source.

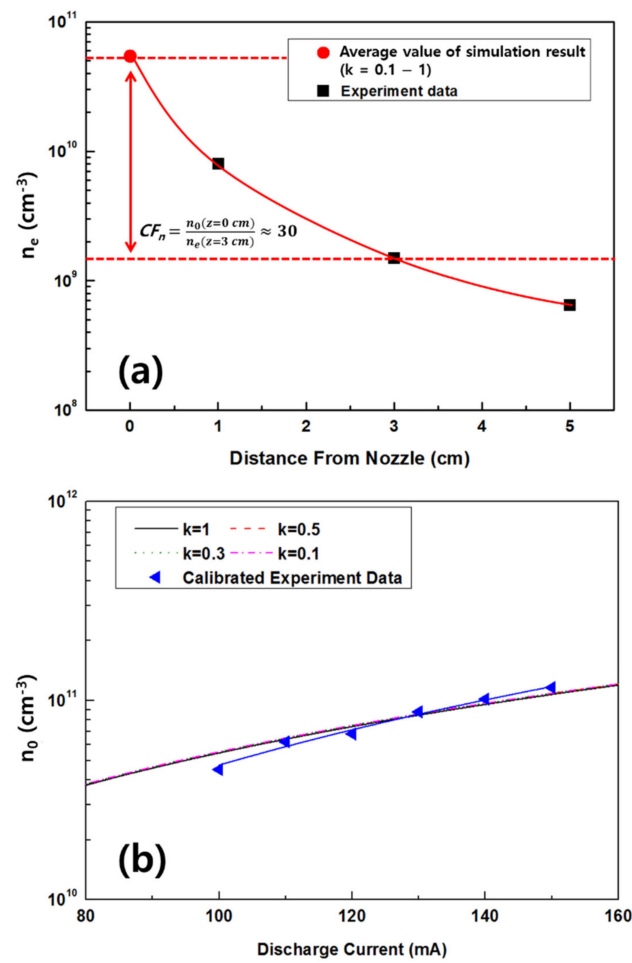


Figure 8. (a) The n_e profiles according to distance from nozzle (argon gas flow rate: 75 sccm) to calibrate position difference for correct comparison of numerical calculation results with experiment data and (b) comparison of numerical calculation results with calibrated experiment data as a function of discharge currents at the same position ($Z: 0$ cm, argon gas flow rate: 75 sccm).

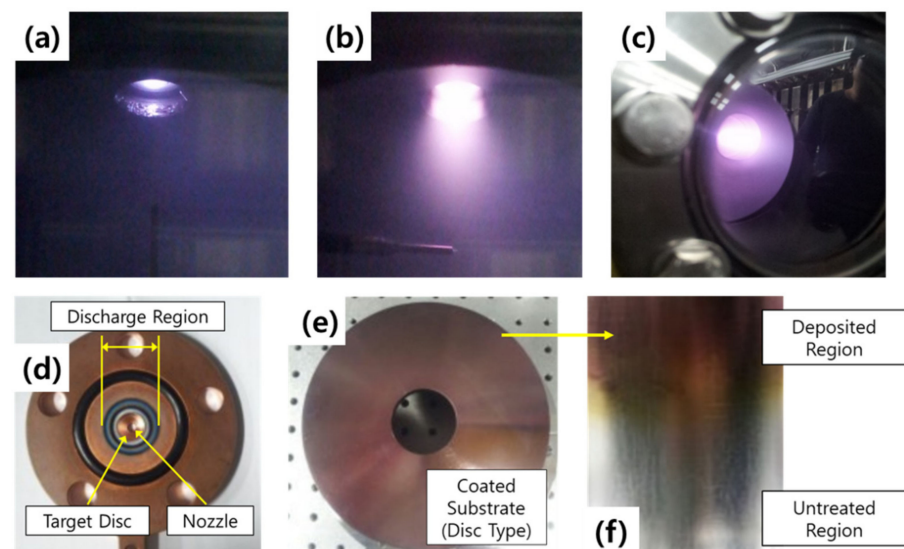


Figure 9. The developed hollow-anode plasma source for material applications: formation of plasma jets by using (a) a DC power (25 W), (b) a pulsed DC power (40 W), (c) RF power (100 W), (d) the used anode and target disc (e) and (f) copper thin films deposited on a stainless steel.

In future works, we will conduct sputtering processes using the developed plasma source and investigate its treatment on various substrates for verification of experimental conditions once more.

5. Conclusions

A new compact plasma jet with the concept of a HAD structure has been developed for an application to sputtering processes. As a DC plasma source, it has a small size with a tiny plasma volume ($R = 60$ mm, $L = 70$ mm, plasma volume = 4×10^3 mm³) and a high plasma density ($n_e \sim 3 \times 10^9$ cm³). It is analyzed by IV curves of discharge, electric probe measurement and numerical analysis with a collisional model. A uniform density discharge model was used to estimate the plasma parameters. To compensate the ideal uniform discharge model with respect to the plausible Gaussian profile of density, a geometry factor (k) was introduced. Plasma jets generated by the developed plasma source were experimentally investigated using voltage–current (VI) characteristics and the measurement of electric probes. After a certain voltage transition, the plasma jets became very stable with a high discharge current, which could be explained by a layered-glow model. By applying $k = 0.1$, T_e became closer to the experimental results than the ideal model and showed similar tendencies, while n_0 seems to be insensitive to the density profile. To compensate for the discrepancy due to the different position of measurement from that of numerical calculations, calibration factors for T_e and n_e are introduced: $CF_T = 4$, $CF_n = 30$, which are to be explained by the decay mechanism of density and temperature along the axial direction in terms of elastic scattering and mean free path. Experimental results with the calibration of position difference for plasma parameters such as T_e and n_0 became very similar to the numerical calculation values at the same position ($z = 0$ cm). With the optimized conditions, the developed HAD source was tested for the deposition of copper thin films, which showed a plausible application to various sputtering processes.

Author Contributions: Conceptualization, I.-J.K. and K.-S.C.; methodology, I.-J.K.; software, I.-J.K. and I.-S.P.; validation, J.-H.K. and K.-S.C.; formal analysis, I.-J.K. and I.-S.P.; investigation, I.-J.K., J.-H.K. and I.-S.P.; data curation, I.-J.K. and K.-S.C.; writing—original draft preparation, I.-J.K.; writing—review and editing, I.-J.K. and K.-S.C.; visualization, I.-J.K.; supervision, J.-H.K. and K.-S.C.; project administration, I.-S.P.; funding acquisition, J.-H.K. and K.-S.C. All authors have read and agreed to the published version of the manuscript.

Funding: This research was supported by R&D Program of “Plasma Convergence & Fundamental Research (1711124796)” through the Korea Institute of Fusion Energy (KFE) and funded by the Government funds, Republic of Korea. This research was supported by the National R&D Program through the National Research Foundation of Korea (NRF) funded by the Ministry of Science, ICT and Future Planning (2019M1A7A1A03088471).

Institutional Review Board Statement: Not applicable.

Informed Consent Statement: Not applicable.

Data Availability Statement: The data presented in this study are available on request from the corresponding author.

Conflicts of Interest: The authors declare no conflict of interest.

References

1. Kang, I.J.; Joa, S.B.; Lee, H.J. Study on effect of plasma surface treatments for diamond deposition by DC arc plasmatron. *J. Nanosci. Nanotechnol.* **2013**, *13*, 7370–7375. [[CrossRef](#)] [[PubMed](#)]
2. Kang, I.J.; Ko, M.G.; Yang, J.K.; Lee, H.J. Plasma surface treatments by using a dielectric barrier discharge for the deposition of diamond films. *J. Korean Phys. Soc.* **2013**, *63*, 199–205. [[CrossRef](#)]
3. Terasawa, T.; Saiki, K. Growth of Graphene on Cu by Plasma Enhanced Chemical Vapor Deposition. *Carbon* **2012**, *50*, 869–874. [[CrossRef](#)]
4. Jeong, J.Y.; Babayan, S.E.; Tu, V.J.; Park, J.; Henins, I.; Hicks, R.F.; Selwyn, G.S. Etching materials with an atmospheric-pressure plasma jet. *Plasma Source Sci. Technol.* **1998**, *7*, 282–285. [[CrossRef](#)]
5. Miljevic, V.I. Hollow anode ion–electron source. *Rev. Sci. Instrum.* **1984**, *55*, 931–933. [[CrossRef](#)]

6. Anders, A.; Anders, S. The working principle of the hollow-anode plasma source. *Plasma Source Sci. Technol.* **1995**, *4*, 571–575. [[CrossRef](#)]
7. Granda-Gutiérrez, E.E.; López-Callejas, R.; Peña-Eguiluz, R.; Valencia, A.R.; Mercado-Cabrera, A.; Barocio, S.R.; de la Piedad-Beneitez, A.; Benítez-Read, J.S.; Pacheco-Sotelo, J.O. V-I curves and plasma parameters in a high density DC glow discharge generated by a current-source. *J. Phys. Conf. Ser.* **2008**, *100*, 062019. [[CrossRef](#)]
8. Abdelsalam, F.W.; Helal, A.G.; Saddeek, Y.B.; Abdelrahman, M.M.; Soliman, B.A. Investigation and application of hollow anode glow discharge ion source. *Nucl. Instrum. Methods Phys. Res. Sect. B* **2010**, *268*, 3464–3467. [[CrossRef](#)]
9. Park, Y.-S.; Hwang, Y.S. Enhancement in ion beam current with layered-glow in a constricted dc plasma ion source. *Rev. Sci. Instrum.* **2010**, *81*, 02B309. [[CrossRef](#)] [[PubMed](#)]
10. Lieberman, M.A.; Lichtenberg, A.J. *Principles of Plasma Discharges and Materials Processing*, 2nd ed.; Wiley: Hoboken, NJ, USA, 2005.
11. Godyak, V.A. *Soviet Radio Frequency Discharge Research*; Delphic: Falls Church, VA, USA, 1986.
12. Kimura, T.; Ohe, K. Global model of inductively coupled Ar plasmas using two-temperature approximation. *J. Appl. Phys.* **2001**, *89*, 4240–4246. [[CrossRef](#)]
13. Chen, F.F. *Introduction to Plasma Physics and Controlled Fusion*, 3rd ed.; Springer: Los Angeles, CA, USA, 2016.
14. Hutchinson, I.H. *Principles of Plasma Diagnostics*, 2nd ed.; Cambridge University Press: New York, NY, USA, 2002.
15. Green, T.S. Beam Formation and Space Charge Neutralisation. *IEEE Trans. Nucl. Sci.* **1976**, *NS-23*, 918–928. [[CrossRef](#)]
16. Abdelsalam, F.W.; Helal, A.G.; Abdelrahman, M.M.; Soliman, B.A. Operating characteristics of the hollow anode glow discharge ion source. *Vacuum* **2010**, *84*, 405–409. [[CrossRef](#)]
17. Chung, K.-S.; Hong, S.-H.; Chung, K.-H. Measurements of Plasma Flow Velocity in DC Plasma Jets Using Perpendicular and Parallel Mach Probes. *Jpn. J. Appl. Phys.* **1995**, *34*, 4217–4222. [[CrossRef](#)]
18. Kim, J.-W.; Cho, S.-G.; Bae, M.-K.; Kim, H.-J.; Chung, T.H.; Chung, K.-S. Analysis of Electron Temperature in DC Ar/SF6 Plasma Using Cylindrical and Planar Probes. *Jpn. J. Appl. Phys.* **2013**, *52*, 11NC03. [[CrossRef](#)]
19. Kang, I.J.; Bae, M.-K.; Lho, T.; Chung, K.-S. Experimental investigation of free and bounded presheaths in weakly magnetized plasmas. *Curr. Appl. Phys.* **2017**, *17*, 358–365. [[CrossRef](#)]
20. Chen, F.F. Langmuir probe analysis for high density plasmas. *Phys. Plasmas* **2001**, *8*, 3029–3041. [[CrossRef](#)]
21. Callen, J.D. *Model of Plasma Confinement and Heating in Tokamaks*; University of Wisconsin: Madison, WI, USA, 1989.
22. Choi, Y.-S.; Woo, H.-J.; Chung, K.-S.; Lee, M.-J. Determination of Plasma Flow Velocity by Mach Probe and Triple Probe with Correction by Laser-Induced Fluorescence in Unmagnetized Plasmas. *Jpn. J. Appl. Phys.* **2006**, *45*, 5945–5950. [[CrossRef](#)]